Force and flux relations for flows of ionic solutions between parallel plates with porous and charged layers

Alexander C. Barbati and Brian J. Kirby*
Sibley School of Mechanical and Aerospace Engineering and Cornell University and Ithaca, New York 14853, USA
(Received 22 May 2013; published 21 October 2013)

We derive coefficients of the electrokinetic coupling matrix (χ_{11}, χ_{12}, and χ_{21}) for the flow of an ionic solution through a parallel-plate geometry having porous and charged layers grafted onto a solid surface with a known potential and demonstrate Onsager reciprocity for the cross terms (i.e., $\chi_{12} = \chi_{21}$). Our results enable the prediction of system outputs in the solid-porous-fluid system from parameters that are either known or may be measured and inferred. These electrokinetic coupling coefficients are in terms of the potential, ϕ, and fixed charge, ρ_f, only, removing dependence on field gradients and fluid velocity. Additionally, we present simplified expressions of these coupling coefficients in limiting regions of the parameter space. Away from these limits, we present numerical results demonstrating the facility of our functional form for facile numerical approximation and report the utility and accuracy of our analytical approximations.

DOI: 10.1103/PhysRevE.88.042408 PACS number(s): 68.08.−p, 47.85.−g, 47.61.−k, 47.56.+r

I. INTRODUCTION

Porous interfaces are ubiquitous in both natural and industrial systems. In nature, vital and nonvital porous structures exist: Organic forms are found within mammalian cells and tissues [1] as biological membranes [2] and cartilage [3,4]. Inorganic porous structures are found in natural geophysical systems like packed silicates [5] and in synthetic components like packed-bed reactors and polymer membranes [6].

A mechanistic understanding of ion transport within membrane and soft-layer systems is required to engineer and optimize device performance. Describing transport within the porous membrane layer requires an understanding of the interplay between chemical and physical attributes of the porous layer. Fuel cells [7], filtration assemblies [8], and electrophoretic [9,10] and chromatography systems with coated surfaces [11] use membranes or membranelike layers to some extent. Contemporary workers use anionic and cationic exchange membranes in through-flow configuration for the purification of brackish solutions [12], where transport across exchange membranes is essential to solution treatment [8].

We consider transport along a porous and charged layer bounded by a solid wall and pure fluid, as shown in Fig. 1. In this figure, the plates are separated by dimension $2h$ and the channel cross section is given by the area $A = 2wh$, with dimension w defining the channel width. The porous layer maintains an immobile charge due to the presence of active chemical groups through its wetted volume and Ohmic conduction results from the electrophoretic motion of cations and anions in the fluid subsumed in the porous layer. Furthermore, the porous layer exhibits a Brinkman-type hydraulic resistivity.

Gradients in pressure and electrical potential combined with a distribution of net free charge give rise to electrokinetic phenomena such as electrophoresis, electroosmosis, streaming potential, streaming current, electrical conductivity, and electroviscosity. Gravitational effects may be included in the pressure [13], i.e., the so-called modified pressure [14], but we do not consider gravitational effects here as they are complicated by the porosity of the medium. These phenomena are linear and additive and are succinctly communicated by the electrokinetic coupling matrix (EKCM). The EKCM describes flux densities of volume and charge through a surface of area A and normal $\vec{n}$ in response to linear gradients in pressure ($\vec{\nabla} p$) and electrical potential ($\vec{\nabla}\phi_{\text{ext}}$).

$$\begin{bmatrix} Q/A \\ I/A \end{bmatrix} = \begin{bmatrix} \chi_{11} & \chi_{12} \\ \chi_{21} & \chi_{22} \end{bmatrix} \begin{bmatrix} -\langle\vec{\nabla} p\rangle \\ -\langle\vec{\nabla}\phi_{\text{ext}}\rangle \end{bmatrix}. \tag{1}$$

The brackets surrounding gradients of pressure and electrical potential in Eq. (1) denote the averaged values of the normal component of vector fluxes taken over the channel cross section,

$$\langle\vec{\nabla}\phi_{\text{ext}}\rangle = \frac{1}{A}\int_S \vec{\nabla}\phi_{\text{ext}} \cdot \vec{n}\, dA, \tag{2}$$

$$\langle\vec{\nabla} p\rangle = \frac{1}{A}\int_S \vec{\nabla} p \cdot \vec{n}\, dA. \tag{3}$$

For the remaining terms in Eq. (1), χ_{11} is the hydraulic conductivity term relating the area-averaged (using the channel cross section) velocity and the pressure gradient; similarly, χ_{12} is the hydraulic conductivity term describing the response to a gradient in electrical potential. The electrical conductivity (both Ohmic and electroosmotic) is given by χ_{22}, and the current produced by a pressure gradient is related through χ_{21}. Exact forms of these coefficients are determined from the geometry and boundary conditions of the system under consideration.

For linear and microscopically reversible processes, the electrokinetic coupling matrix is symmetric. This is a statement of Onsager reciprocity [15–18]; holding so long as, for a near-equilibrium system, the forces and the fluxes relate linearly, and the system remains symmetric upon time reversal. These requirements for Onsager reciprocity generally hold, broken only, for example, when the system considered is placed under the action of a magnetic field or subject to a Coriolis force. Systems so exposed will not reverse in time

*bk88@cornell.edu; http://www.kirbyresearch.com

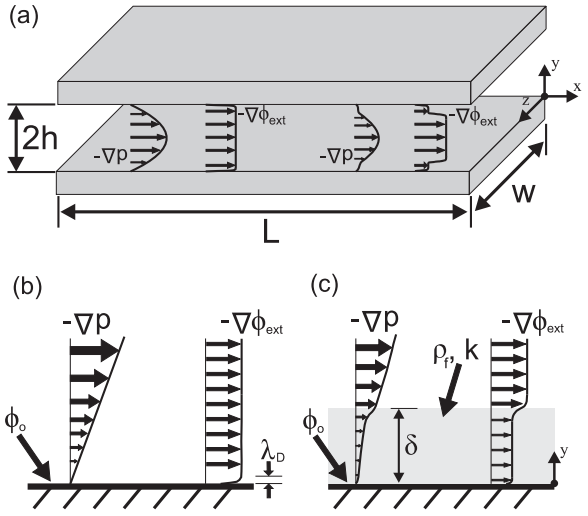

FIG. 1. Diagrammatic representation of the system under consideration. (a): Geometric definition of the parallel-plate system studied; plates of width w and length L are separated by a distance $2h$. Included are shapes of pressure-driven and electrically forced flows for (left) a channel with rigid surfaces and (right) a channel with a porous lining. In (b) and (c), magnified diagrams at the surface detail distributions of velocity and potential for a bare, rigid surface (b) and a surface with a porous layer of thickness δ (c).

and will not exhibit reciprocity in the coefficients describing forces and fluxes [17].

Statements of Onsager reciprocity applied to electrokinetic systems are known in the interface and microfluidic literature. Similarly to thermoelectric phenomena, reciprocal relationships were known long before the phenomena were codified theoretically. In 1892 Saxén demonstrated the equivalence between electroosmosis and streaming potential [19], showing $\chi_{12} = \chi_{21}$ experimentally. This work was followed by contributions [20,21] examining the equivalence between porous diaphragms and networks of capillaries. More contemporary work by Gross and Osterle [22] discusses coupling relationships in capillary flow, contributing general integral expressions for pressure, electrical, and chemical potential gradients driving fluxes of volume, current, and mass; with attention to electrodialysis and energy conversion. Extending these ideas to arbitrarily shaped ducts, Mortensen *et al.* [23] develop expressions for the EKCM coefficients using a Hilbert space, also showing Onsager reciprocity for the cross terms. The early history of equivalence between electroosmosis and streaming potential is discussed in a review by Wall [24].

More recent investigations have moved beyond pure fluids bounded by rigid, nonreacting surfaces. Brunet and Ajdari [25] have developed a general derivation proving the symmetry property of a coupling matrix for systems with arbitrary microstructure. In their formulation, the system need only obey the no-slip boundary condition, exhibit Newtonian Stokes flow, and obey the Poisson equation for potential in response to a spatial free charge density. They simplify their general results for a periodic isotropic medium and show that the Onsager reciprocal relation holds. Brunet and Adjardi do not, however, present functions for the coupling coefficients. In fact, their proof omits definition of electrical boundary conditions (charge and/or potential) on the system walls. Berli and Olivares [26] develop expressions for electrokinetic coupling coefficients in systems where the working fluid is non-Newtonian. They report symmetry in the electrokinetic coupling matrix, although their model prohibits nonlinear viscosity in regions of nonzero electrical potential, the assertion being that the depletion zone of a polymer additive causing the nonlinear flow effects is thicker than the region of net charge. Also, their system ceases to be strictly linear for non-Newtonian fluids, as coefficient χ_{11} will contain a pressure dependence. van Leeuwen and Duval [27] describe effects of a conductive substrate, where faradaic reactions are permitted, on the form of Onsager relations.

Previous works have considered coupling coefficients in channels with charged and porous layers. Donath and Voigt [28] present a 1D formulation of the system we consider, although their approach assumes a low-potential limit and incorrectly predicts a divergence in streaming current as the Debye length of the solvent approaches the characteristic penetration length of the free fluid into the porous region (in our notation, $\lambda_D \to \lambda_o$). A similar approach was taken by Ohshima and Kondo [29], deriving approximate forms for χ_{12} and χ_{21} (confirming Onsager reciprocity) for a channel many times larger than both the fluid Debye length and the penetration depth of fluid into the porous region. Keh and Liu [30] derive exact analytical expressions for coupling coefficients for the linearized Poisson-Boltzmann equation in a cylindrical geometry. A pair of articles, by Duval and van Leeuwen [31] and Duval [32], develop electrokinetic theories for porous regions of nonuniform charge and resistance, relaxing an assumption of previous workers; results are presented for the small-potential (linearized) regime [31], as well as the nonlinear regime [32]. In a recent publication, we have reviewed electrokinetics of soft and charged layers from both theoretical and experimental viewpoints [33].

In this work, we develop general, closed-form integral expressions describing electrokinetic transport over and within porous layers of uniform resistance and arbitrary fixed charge density; these integral expressions require only physicochemical porous layer properties such as porous layer resistance, porous layer thickness, the distribution of the fixed charge, and the electrical potential in the system. Our results do not require knowledge of the potential gradient or velocity within the channel (other than velocity boundary conditions). Often, these required quantities may be approximated. Generally, the values of potential and charge can be reliably computed. In contrast to previously published results, our expression for the cross-coupling term applies for arbitrary values of the fixed charge density, and geometric and resistive parameters, without regard to the magnitude of the electrical potential in the system. This general integral formulation also facilitates our derivation of simple limiting forms that apply accurately across a wide range of parameter space.

The paper is organized as follows: in Sec. II, we describe fluid physics in porous layers. In Sec. III, we describe generating formulas for all electrokinetic phenomena, incorporating domain inhomogeneities introduced in the previous section. Coupling formulas are then applied to systems with a hard surface in Sec. IV. These results are contrasted with (and used to motivate) the porous layer coupling coefficients we derive

and present in Sec. V. In Sec. VI, we derive limiting cases of porous layer coefficients, and in Sec. VII, we present numerical representations of coefficients for cases not described by simplifying limits.

II. FLUID PHYSICS IN POROUS LAYERS

We consider momentum transport at low Reynolds number, governed by the Stokes equation of motion. Fluid forcing in the Stokes equations is linear and additive: Gradients in pressure or external electrical potential actuate the fluid independently, and solutions for flows driven by gradients of pressure or electric fields may be superimposed. In the pure-fluid region,

$$0 = \eta\vec{\nabla}^2\mathbf{u} - \vec{\nabla}p - \rho_e\vec{\nabla}\phi_{\text{ext}}. \tag{4}$$

Here η is the fluid viscosity, $\mathbf{u}$ is the velocity field, and ρ_e is the free charge density. Equation (4) holds outside of the porous layer. Within the porous layer, we add a term linear in the velocity which accounts for the added resistance of the porous layer beyond the unbounded fluid,

$$0 = \eta\vec{\nabla}^2\mathbf{u} - k\mathbf{u} - \vec{\nabla}p - \rho_e\vec{\nabla}\phi_{\text{ext}}. \tag{5}$$

The constant, k, describes the resistivity of the porous region. In both Eqs. (4) and (5), gradients in pressure and external electrical potential are equivalent in the porous layer and pure fluid.

Multiple schemes have been proposed to connect porous layer and pure fluid flows; we use the Brinkman approach because of the ability to obey both boundary conditions in the porous layer, as well as the ubiquity of the Brinkman approach for the type of problem that we consider here. The Brinkman approach to the momentum distribution is widely used for planar (or nearly planar) porous layers between a solid surface and pure fluid [28,30–32,34–39] and has been reviewed in this context by Dukhin *et al.* [40]. Although we work with the Brinkman-modified Stokes equation to connect the porous-layer and pure-fluid flows, coupling between free-fluid and porous layer flows may also be done using the Beavers-Joseph boundary condition [41]; both approaches are approximate and exhibit deficiencies in predicting the velocity profile at the interface between the porous and pure-fluid phases and have been the subject of much discussion [13,42–46]. Although the Beavers-Joseph condition matches the velocity at the porous layer-fluid interface, it assumes a Darcian flow inside the porous layer and does not explicitly obey the no-slip condition at the solid wall-porous medium boundary. Although this may be unimportant for macroscale systems (porous layer thickness $\ll\sqrt{\frac{\eta}{k}}$) with low porosity, we consider systems with porous layers that may be thin relative to $\sqrt{\frac{\eta}{k}}$, requiring that the no-slip condition at the solid boundary be obeyed.

Equations (4) and (5) are typically solved in response to a single momentum source. We indicate forcing with superscripts: $\mathbf{u}^{(p)}$ for pressure-driven flow and $\mathbf{u}^{(e)}$ for flows driven by electric fields. Furthermore, we label the velocity in the porous layer with subscript 1, i.e., $\mathbf{u}_1^{(p)}$, and in the fluid with subscript 2, as $\mathbf{u}_2^{(p)}$.

Momentum distributions in the porous layer and in the pure fluid connect via boundary conditions. For the one-dimensional geometry we consider (Fig. 1), a no-slip condition is applied at the fluid-solid interface, and a symmetry condition is imposed at the channel centerline. The boundary conditions at the interface between the porous and pure-fluid regions require continuity of velocity and stress as follows:

$$u_1(0) = 0 \quad u_1(\delta) = u_2(\delta)$$
$$\left.\frac{du_1}{dy}\right|_{y=\delta} = \left.\frac{du_2}{dy}\right|_{y=\delta} \quad \left.\frac{du_2}{dy}\right|_{y=h} = 0. \tag{6}$$

Here, the Brinkman resistance term $-ku$ is absent, as the boundary conditions are dominated by the tangential stresses; the Brinkman resistance acts on a fluid volume and is lost in the limiting process.

The free charge distribution is determined from the Poisson equation with a fixed-charge that is zero in the pure fluid and nonzero in the porous layer. In general,

$$\vec{\nabla}\cdot(-\varepsilon\varepsilon_o\vec{\nabla}\phi) = \rho_e(\mathbf{x}) + \rho_f(\mathbf{x}). \tag{7}$$

Here, the distribution of fixed charge is given by $\rho_f(\mathbf{x})$ and may exhibit a dependence on the potential. The electrical potential distribution is determined by the form of the free charge density, ρ_e, the distribution of fixed charge in the domain, ρ_f, and boundary conditions. The dielectric constant of the solvent is given by ε, and ε_o is the vacuum permittivity. The pure-fluid phase cannot support a fixed charge distribution, so $\rho_f = 0$ in this region of the domain,

$$\vec{\nabla}\cdot(-\varepsilon\varepsilon_o\vec{\nabla}\phi_2) = \rho_e(\mathbf{x}). \tag{8}$$

Again, we use the subscript 2 to indicate quantities in the pure-fluid region of the domain. The porous layer is the only region with nonzero fixed charge density. Fixed charges reside throughout the wetted volume of the porous material. In the porous region,

$$\vec{\nabla}\cdot(-\varepsilon\varepsilon_o\vec{\nabla}\phi_1) = \rho_e(\mathbf{x}) + \rho_f(\mathbf{x}). \tag{9}$$

The potential distributions in Eqs. (8) and (9) also couple through boundary conditions. We prescribe a fixed potential on the hard boundary at $y = 0$ and zero potential slope at the channel centerline. At the interface between the fluid and porous layer, continuity in potential and electric flux density, for uniform permittivity, implies matching potential and potential gradient as follows:

$$\phi_1(0) = \phi_o \quad \phi_1(\delta) = \phi_2(\delta)$$
$$\left.\frac{d\phi_1}{dy}\right|_{y=\delta} = \left.\frac{d\phi_2}{dy}\right|_{y=\delta} \quad \left.\frac{d\phi_2}{dy}\right|_{y=h} = 0. \tag{10}$$

Equality between dielectric constants in the pure-fluid and porous regions is implicitly assumed in the field gradient relation. This constraint was relaxed by Ohshima and Ohki [47] in their analysis of potential profiles across charged biological membranes.

The free-charge density depends upon the local concentration of ions. Typically, a mean-field approximation is used to relate the free-charge density to the potential. By further considering the free ions as point charges, we arrive at the Boltzmann relation for the free-charge density [48]:

$$\rho_e(\mathbf{x}) = F\sum_i z_i c_{i,\infty} e^{-\frac{z_i F\phi(\mathbf{x})}{RT}}. \tag{11}$$

Here R is the ideal gas constant, T the absolute temperature, F is Faraday's constant, and z_i and $c_{i,\infty}$ are the valence and bulk concentration of the i^{th} ionic component.

The potential within a porous layer at a point where free and fixed charges exactly balance is known as the Donnan potential [49] and implies that the potential is curvature-free. The functional form connecting the Donnan potential to the fixed-charge distribution depends upon the form of the free- and fixed-charge densities. For a fixed charge density that is independent of the local potential, and a free charge determined by (11),

$$0 = F\sum_j z_j c_{j,\infty} e^{-\frac{z_j F\phi_D}{RT}} + \rho_f(\mathbf{x}). \tag{12}$$

For a z:z electrolyte, Eq. (12) has the form $\phi_D = \frac{RT}{zF}\text{arcsinh}(\frac{\rho_f(\mathbf{x})}{2zFc_\infty})$, where ϕ_D denotes the Donnan potential in the porous layer.

III. GENERATING INTEGRAL FORMULAS FOR EKCM COEFFICIENTS

All electrokinetic coupling coefficients may be expressed in a general integral form. Typically, the EKCM coefficients are calculated with direct integration in only the simplest systems, but these forms are the starting point for expressions that we derive in later sections. We write an integral expression for χ_{11} for a pressure-driven flow that proceeds through a surface S with unit normal $\vec{n}$ and corresponding flow field $\mathbf{u}^{(p)}(\mathbf{x})$ as follows:

$$\chi_{11} = \frac{1}{\int_S -\vec{\nabla}p\cdot\vec{n}\,dA}\int_S \mathbf{u}^{(p)}(\mathbf{x})\cdot\vec{n}\,dA. \tag{13}$$

Terms χ_{12} and χ_{21} relate the area-averaged volume and current fluxes to the application of external electrical potential and pressure gradients, respectively. The general forms of these expressions are given by

$$\chi_{12} = \frac{1}{\int_S -\vec{\nabla}\phi_{\text{ext}}\cdot\vec{n}\,dA}\int_S \mathbf{u}^{(e)}(\mathbf{x})\cdot\vec{n}\,dA, \tag{14}$$

$$\chi_{21} = \frac{1}{\int_S -\vec{\nabla}p\cdot\vec{n}\,dA}\int_S \rho_e(\mathbf{x})\mathbf{u}^{(p)}(\mathbf{x})\cdot\vec{n}\,dA. \tag{15}$$

The symbols $\rho_e(\mathbf{x})$, $\mathbf{u}^{(e)}(\mathbf{x})$, and $-\vec{\nabla}\phi_{\text{ext}}$ denote the free-charge density, electric-field-driven flow, and the electric field. In the above expressions, gradients in pressure and electrical potential are assumed uniform across the surface S.

The final term, χ_{22}, relates the area-averaged current to the applied electrical potential gradient. We refer to this as the conductivity term. In general form, we write this as

$$\chi_{22} = \sigma_{\text{Ohmic}} + \sigma_{\text{Ohmic}}^{(\text{ex})} + \sigma_{\text{EO}}^{(\text{ex})}. \tag{16}$$

We have separated the conductivity term into three components. The bulk conductivity, σ_{Ohmic}, represents the contribution from Ohmic conduction. Contributions to Ohmic conductivity from boundary effects are included in $\sigma_{\text{Ohmic}}^{(\text{ex})}$. We have used the superscript (ex) to indicate excess or surface contributions to the system conductivity. Finally, the electroosmotic contribution, $\sigma_{\text{EO}}^{(\text{ex})}$, represents the contribution by electroosmotic transport of current when a field is applied. In integral form,

$$\sigma_{\text{Ohmic}} = \frac{1}{\int_S \vec{\nabla}\phi_{\text{ext}}\cdot\vec{n}\,dA}F\sum_i |z_i|\,\mu_i\int_S c_{i,\infty}\vec{\nabla}\phi_{\text{ext}}\cdot\vec{n}\,dA, \tag{17}$$

$$\sigma_{\text{Ohmic}}^{(\text{ex})} = \frac{1}{\int_S \vec{\nabla}\phi_{\text{ext}}\cdot\vec{n}\,dA}F\sum_i |z_i|\mu_i \times\int_S (c_i(\mathbf{x})-c_{i,\infty})\vec{\nabla}\phi_{\text{ext}}\cdot\vec{n}\,dA, \tag{18}$$

$$\sigma_{\text{EO}}^{(\text{ex})} = \frac{1}{-\int_S \vec{\nabla}\phi_{\text{ext}}\cdot\vec{n}\,dA}\int_S \rho_e(\mathbf{x})\mathbf{u}^{(e)}(\mathbf{x})\cdot\vec{n}\,dA. \tag{19}$$

The symbol μ_i represents the mobility of the i^{th} ion. In most microfluidic systems, the excess conductivities are small when the double layers are thin relative to the system size.

IV. COUPLING TERMS FOR SYSTEMS WITH RIGID INTERFACES

We present coupling terms for a parallel-plate system with bare rigid walls as a prelude to the porous layer geometry. These terms are dependent on the potential distribution and do not require explicit details of the flow as inputs beyond boundary conditions and the forces applied to the fluid (pressure or electrical potential). Furthermore, simplifications and physical insight proceed quickly from the integral forms of the coupling terms. Here, the flow u proceeds along the x direction and varies across the half domain $0 \leqslant y \leqslant h$. At the solid boundary, we fix the potential, ϕ_o, and enforce a no-slip boundary condition. At the channel centerline, both velocity and potential obey a homogeneous Neumann condition. Equations (4) and (8) reduce from partial to ordinary differential equations as follows:

$$\frac{dp}{dx} = \eta\frac{d^2u}{dy^2}, \tag{20}$$

$$-\varepsilon\varepsilon_o\frac{d^2\phi}{dy^2} = \rho_e(y). \tag{21}$$

The hydraulic resistance term, χ_{11}, is determined from Eqs. (20) and (13) along with no-slip boundary conditions,

$$\chi_{11}^{(\text{hard})} = \frac{h^2}{3\eta}. \tag{22}$$

The current density in response to a pressure gradient is computed from

$$\chi_{21}^{(\text{hard})} = \frac{1}{-\langle\vec{\nabla}p\rangle A}\int_0^{2h}\int_0^w u^{(p)}\rho_e(y)\,dzdy. \tag{23}$$

Here $0 \leqslant z \leqslant w$ is the channel width (into the page, in Fig. 1). We assume that the velocity, potential, and charge profiles are uniform in this direction. With $A = 2hw$,

$$\chi_{21}^{(\text{hard})} = \frac{1}{-h\langle\vec{\nabla}p\rangle}\int_0^h u\left(-\varepsilon\varepsilon_o\frac{d^2\phi}{dy^2}\right)dy. \tag{24}$$

After integration by parts (twice), enforcing boundary conditions $u(0) = 0$ (no slip), $\phi(0) = \phi_o$, $\frac{du}{dy}|_{y=h} = \frac{d\phi}{dy}|_{y=h} = 0$

(symmetry), and finding the velocity gradient at the wall,

$$\chi_{21}^{(\mathrm{hard})} = -\frac{\varepsilon\varepsilon_o\phi_o}{\eta}\left[1 - \frac{1}{h}\int_0^h \frac{\phi(y)}{\phi_o}\,dy\right]. \tag{25}$$

To find the flux density of volume in response to an applied electric field, absent pressure gradients, we compute

$$\chi_{12}^{(\mathrm{hard})} = \frac{2\int_0^h u^{(e)}\,dy}{-2wh\langle\vec{\nabla}\phi_{\mathrm{ext}}\rangle} = -\frac{1}{h\langle\vec{\nabla}\phi_{\mathrm{ext}}\rangle}\int_0^h u^{(e)}\,dy. \tag{26}$$

The solution is most easily obtained by solving directly for the field $\mathbf{u}^{(e)}$ from the Stokes equations with zero pressure forcing, a no-slip boundary, and symmetrical velocity profiles about the centerline

$$\chi_{12}^{(\mathrm{hard})} = -\frac{1}{h\langle\vec{\nabla}\phi_{\mathrm{ext}}\rangle}\int_0^h \frac{\varepsilon\varepsilon_o}{\eta}\langle\vec{\nabla}\phi_{\mathrm{ext}}\rangle\,(\phi_o - \phi(y))\,dy \tag{27}$$

or

$$\chi_{12}^{(\mathrm{hard})} = -\frac{\varepsilon\varepsilon_o}{\eta}\phi_o\left[1 - \frac{1}{h}\int_0^h \frac{\phi}{\phi_o}\,dy\right]. \tag{28}$$

The conductivity term is more complicated, owing to the convolution of the charge density and electroosmotic flow; both terms have a direct connection with the electrical potential. Using earlier results, we express the conductivity for our 1D flow as

$$\chi_{22}^{(\mathrm{hard})} = F\sum_i |z_i|\,\mu_i\frac{1}{h}\int_0^h c_i(y)\,dy - \frac{\int_0^h \rho_e(y)u^{(e)}(y)\,dy}{h\langle\vec{\nabla}\phi_{\mathrm{ext}}\rangle}. \tag{29}$$

The excess conductivity $(\sigma_{\mathrm{EO}}^{(\mathrm{ex})} + \sigma_{\mathrm{Ohmic}}^{(\mathrm{ex})})$ has been determined by Bikerman for $h \gg \lambda_D$ and a symmetric electrolyte [50], which we reproduce here under the additional assumption of balanced mobilities for the electrolyte pair,

$$\begin{aligned}\chi_{22}^{(\mathrm{hard})} &= \sigma_{\mathrm{Ohmic}} + \frac{\lambda_D}{h}\frac{2F^2c_\infty z^2 D}{RT}\left(1 + \frac{3m}{z^2}\right)\\ &\quad\times\left[\cosh\left(\frac{zF\phi_o}{2RT}\right) - 1\right]\\ &= \sigma_{\mathrm{Ohmic}} + \frac{2\varepsilon\varepsilon_o D}{h}\left(1 + \frac{3m}{z^2}\right)\\ &\quad\times\left[\cosh\left(\frac{zF\phi_o}{2RT}\right) - 1\right].\end{aligned} \tag{30}$$

Of critical significance is the parameter $m = (\frac{RT}{F})^2\frac{2\varepsilon\varepsilon_o}{3\eta D}$, which relates the relative contributions of excess Ohmic and electroosmotic conductivities: $\sigma_{\mathrm{Ohmic}}^{(\mathrm{ex})} = \frac{3m}{z^2}\sigma_{\mathrm{EO}}^{(\mathrm{ex})}$. Simplified relationships for the conductivity outside of the $h \gg \lambda_D$ limit are not available; in such cases we represent excess Ohmic and electroosmotic conductivities in integral form, written here assuming a Boltzmann distribution for the free-charge density,

$$\sigma_{\mathrm{Ohmic}}^{(\mathrm{ex})} = F\sum_i |z_i|\,\mu_i c_{i,\infty}\frac{1}{h}\int_0^h \left(e^{-\frac{z_iF\phi(y)}{RT}} - 1\right)dy, \tag{31}$$

$$\begin{aligned}\sigma_{\mathrm{EO}}^{(\mathrm{ex})} &= \frac{(\varepsilon\varepsilon_o)^2}{\eta}\frac{1}{h}\int_0^h\left(\frac{d\phi}{dy}\right)^2 dy\\ &= 2\frac{\varepsilon\varepsilon_o RT}{\eta h}\sum_i c_{i,\infty}\int_0^h\left(e^{-\frac{z_iF\phi(y)}{RT}} - e^{-\frac{z_iF\phi_{\mathrm{mid}}}{RT}}\right)dy.\end{aligned} \tag{32}$$

Outside the thin electrical double layer limit, the potential at the channel centerline is nonzero, represented here by ϕ_{mid}. We do not consider the conductivity further in this work.

A. Remarks on coupling terms for rigid interfaces

The results derived in this section are general: In χ_{11} we assume only that the fluid is Newtonian with no-slip boundaries. Examining the cross terms, χ_{12} and χ_{21}, we observe a term depending only on the electrical boundary condition and an integral term representing the average channel potential; this integral term is proportional to the ratio $\frac{1}{h}$, and, since the potential varies appreciably only over λ_D, the contribution of this integral term will be minimal when $\lambda_D \ll h$. Finally, the χ_{12} and χ_{21} relations apply for *all forms* of the charge distribution—the relations do not require a point-charge or other approximation; hard-sphere corrections, for example, may be included. These remarks indicate that for systems with $h \gg \lambda_D$, χ_{12} and χ_{21} depend chiefly upon the boundary value, and details of the mobile or free charge distribution may be omitted.

The conductivity term, $\chi_{22}^{(\mathrm{hard})}$, is the least general, requiring free-charge and electroosmotic distributions that must be integrated. Because the excess conductivities are localized to regions near the charged surface, the importance of these excess conductivities diminish as the size of the system (i.e., h) increases.

V. COUPLING TERMS FOR SYSTEMS WITH POROUS AND CHARGED INTERFACES

Porous and charged layers affect both electrical potential and momentum distributions. A system with a porous layer has increased hydraulic resistance in the porous region, as captured in the Stokes-Brinkman equation by the added term $-k\mathbf{u}$. Porous and charged layers contribute a fixed charge density term in the Poisson equation, $\rho_f(\mathbf{x})$. For the parallel-plate system considered here, the differential equations for the porous layer ($0 \leqslant y \leqslant \delta$) become

$$0 = \eta\frac{d^2u}{dy^2} - ku - \frac{dp}{dx} - \frac{d\phi_{\mathrm{ext}}}{dx}\rho_e, \tag{33}$$

$$-\varepsilon\varepsilon_o\frac{d^2\phi}{dy^2} = \rho_e(y) + \rho_f(y). \tag{34}$$

Outside of the porous layer of thickness δ ($y \geqslant \delta$), we solve Eqs. (20) and (21). These equations are coupled by the boundary conditions presented in (6) and (10).

A. χ_{11} with porous and charged interfaces

A porous layer reduces the hydraulic conductance of the channel. The porous layer exhibits a resistance beyond the viscous retardation of the fluid alone; this effect is captured

in the $-ku$ term. Below, we solve for the velocity in the channel and then describe the hydraulic conductance, $\chi_{11}^{(\mathrm{soft})}$. For convenience and clarity, we work in the dimensionless variable $y^* = y/\delta$ and define $\beta = h/\delta$, which is the half-height of the channel normalized by the porous layer thickness. We introduce parameters $\lambda_o = \sqrt{\frac{\eta}{k}}$, a measure of the penetration of momentum from the pure fluid into the porous layer, $\alpha = \frac{\delta}{\lambda_o}$, to characterize the thickness of the porous layer relative to the penetration distance of momentum from the pure fluid into the porous layer, and $G = \frac{\delta^2}{\eta}\langle\vec{\nabla}p\rangle$, a modified pressure gradient with units of velocity.

The shape of the velocity profiles are strong functions of α and β. Equations (35) and (36) show the nonlinear dependence in the parameter α as follows:

$$u_1^{(p)} = \frac{G}{\alpha^2}\left(\cosh(\alpha y^*) - 1 - \frac{\sinh(\alpha y^*)}{\cosh(\alpha)} \times [\alpha(\beta-1) + \sinh(\alpha)]\right), \tag{35}$$

$$u_2^{(p)} = \frac{G}{\alpha^2}\left(\frac{1}{\cosh(\alpha)} + \frac{\alpha^2}{2}(y^*-1)(1+y^*-2\beta) - 1 - \alpha(\beta-1)\tanh(\alpha)\right). \tag{36}$$

These equations are plotted in Fig. 2, showing the velocity profiles across the channel for small, moderate, and large resistance parameters (α). Perturbations induced by the porous layer on the momentum distribution are dependent on β, mostly by constriction effects, as α becomes large. For values of β approaching unity, nearly all nonvanishing values of α will have some effect on the velocity profiles.

For the one-dimensional geometry considered, we compute $\chi_{11}^{(\mathrm{soft})}$ from Eq. (13). This yields

$$\chi_{11}^{(\mathrm{soft})} = \frac{h^2}{3\eta}\left[1 - \frac{3\alpha^2\beta^2 - 3\alpha^2\beta + \alpha^2 - 6\beta + 3}{\alpha^2\beta^3} - \frac{6(\beta-1)}{\alpha^2\beta^3\cosh(\alpha)} + 3\left(\frac{(\beta-1)^2}{\alpha} - \frac{1}{\alpha^3}\right)\frac{\tanh(\alpha)}{\beta^3}\right]. \tag{37}$$

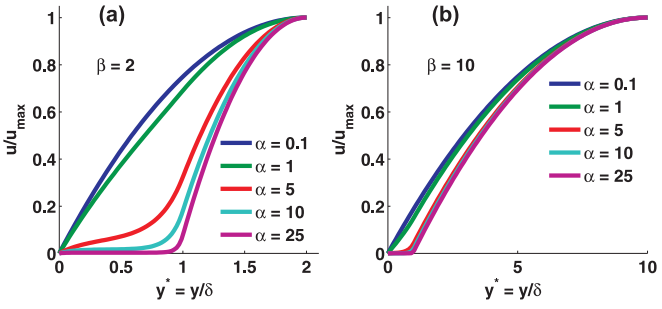

FIG. 2. (Color online) Velocity profiles about the channel centerline for varying layer resistance parameter α and relative channel height β. At left, $\beta = 2$, the velocity profile is strongly perturbed from parabolicity by large and moderate values of α. At right, $\beta = 10$, the channel is large relative to the porous layer thickness, and retarding effects are mainly confined to the porous layer and do not interfere strongly with momentum transport in the pure fluid region.

In addition to the nondimensional parameters α and β, Eq. (37) contains two dimensional parameters, the domain height, h, and the viscosity, η. The premultiplying dimensional term is the exact result for the hydraulic conductivity between two parallel plates; the additional bracketed terms represent corrections due to the thickness and resistivity of the porous layer.

Similarly to the velocity profiles just described, $\chi_{11}^{(\mathrm{soft})}$ is strongly dependent on α. For a porous region that is greatly resistive, $\alpha \gg 1$,

$$\frac{\chi_{11}^{(\mathrm{soft})}}{h^2/3\eta} = 1 - \frac{3\beta^2 - 3\beta + 1}{\beta^3} + \frac{3(\beta-1)^2}{\alpha\beta^3} + O\left(\frac{1}{\alpha^2}\right). \tag{38}$$

In this limit, transport within the porous layer is diminished, and the porous layer serves to constrict the channel volume. If the porous layer becomes impenetrable ($\alpha \to \infty$),

$$\frac{\chi_{11}^{(\mathrm{soft})}}{h^2/3\eta} = 1 - \frac{3\beta^2 - 3\beta + 1}{\beta^3}. \tag{39}$$

For a porous region that is weakly resistive, $\alpha \ll 1$, we describe this layer using a series expansion in the now-small parameter α,

$$\frac{\chi_{11}^{(\mathrm{soft})}}{h^2/3\eta} = 1 - \frac{3 - 5\beta(3-4\beta)}{20\beta^3}\alpha^2 + O(\alpha^4). \tag{40}$$

A vanishingly small resistance corresponds to a porous layer with no resistance beyond the viscosity of the working fluid and is equivalent to the limit $\alpha \to 0$. In this case,

$$\frac{\chi_{11}^{(\mathrm{soft})}}{h^2/3\eta} = 1. \tag{41}$$

Both large- and small-α limits concur with physical intuition. For a very resistive layer, the channel is throttled by the impermeable porous layer and a reduced channel height. For a "porous" layer with zero resistance, $\chi_{11}^{(\mathrm{soft})}$ has no dependence on the layer thickness δ, as the porous layer provides no additional resistance to the channel. Between these limits, the hydraulic conductivity varies smoothly across a large range of α. This behavior is shown in Fig. 3.

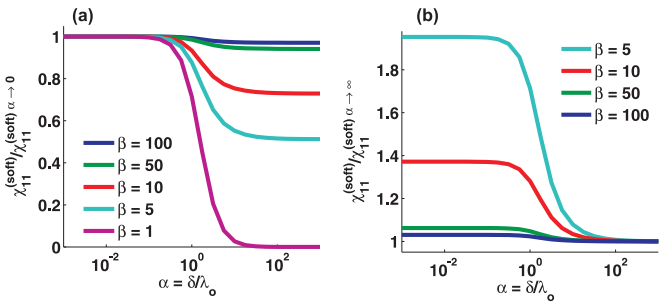

FIG. 3. (Color online) Plots of $\chi_{11}^{(\mathrm{soft})}$ normalized by the $\alpha \to 0$ limit (left) and the $\alpha \to \infty$ limit (right). In both cases, porous layer effects are small when the channel height is large relative to the porous layer thickness ($\beta \gg 1$).

B. χ_{21} with porous and charged interfaces

The current density in response to a pressure gradient is related through the coupling coefficient $\chi_{21}^{(\mathrm{soft})}$, which is a convolution of the pressure-driven velocity field and the total charge density formed by mobile ions. In the presence of a permeable layer with fixed charge, the magnitude of convected charge can differ markedly from the rigid interface previously considered. There are two sources for this change: (1) the distribution of ions is perturbed by the porous and charged layer and (2) the distribution of momentum is perturbed by the porous and charged layer.

We derive $\chi_{21}^{(\mathrm{soft})}$ in a general form, accounting for a uniformly resistive porous layer. Our derivation places no requirements on the distribution of charge, nor do we assume a distribution (or magnitude) of potential (beyond that which solves a general Poisson equation). Thus, our formulation assumes only the existence of potential and fixed-charge distributions.

For the parallel-plate geometry, we derive $\chi_{21}^{(\mathrm{soft})}$ by substituting in the Poisson equation and the known velocity solution and repeatedly integrating by parts. We start with the following:

$$\chi_{21}^{(\mathrm{soft})} = \frac{I/A}{-\langle\vec{\nabla}p\rangle} = -\frac{1}{\beta\langle\vec{\nabla}p\rangle}\int_0^\beta u^{(p)}\rho_e\,dy^*. \tag{42}$$

Here, and in the following Poisson equation, we again scale the spatial coordinate y by the porous layer thickness δ,

$$-\frac{\varepsilon\varepsilon_o}{\delta^2}\frac{d^2\phi}{dy^{*2}} = \rho_e(y^*) + \rho_f(y^*). \tag{43}$$

By substituting out the charge density in (42) for the potential curvature and fixed charge density terms, we obtain the following:

$$-\frac{1}{\beta\langle\vec{\nabla}p\rangle}\int_0^\beta u^{(p)}\left(-\frac{\varepsilon\varepsilon_o}{\delta^2}\frac{d^2\phi}{dy^{*2}} - \rho_f(y^*)\right)dy^* = \frac{1}{\beta\langle\vec{\nabla}p\rangle}\left[\frac{\varepsilon\varepsilon_o}{\delta^2}\int_0^\beta u^{(p)}\frac{d^2\phi}{dy^2}\,dy^* + \int_0^1 u^{(p)}\rho_f(y^*)\,dy^*\right]. \tag{44}$$

The limits of the last integral range only from $0 \leqslant y^* \leqslant 1$, because ρ_f vanishes outside the porous layer. After successive integrations by parts, and invoking the boundary conditions on velocity and potential,

$$\chi_{21}^{(\mathrm{soft})} = \frac{\varepsilon\varepsilon_o}{\eta}\phi_o\left[\frac{1}{\beta G}\frac{du_1^{(p)}}{dy^*}\bigg|_{y^*=0} + \frac{1}{\beta}\int_0^\beta\frac{\phi}{\phi_o}\,dy^* + \frac{1}{\beta}\int_0^1\frac{u_1^{(p)}}{\alpha^2 G}\left(\frac{\phi}{\phi_o} + \frac{\delta^2}{\alpha^2\varepsilon\varepsilon_o}\frac{\rho_f}{\phi_o}\right)dy^*\right]. \tag{45}$$

The velocity in the porous layer is known and described in the previous section. The velocity gradient at the boundary between the rigid wall and porous layer is $\frac{du_1^{(p)}}{dy^*}|_{y^*=0} = G(\frac{1-\beta}{\cosh(\alpha)} - \frac{\tanh(\alpha)}{\alpha})$. Including these terms gives

$$\begin{aligned}\chi_{21}^{(\mathrm{soft})} = -\frac{\varepsilon\varepsilon_o}{\eta}\phi_o\Bigg[&\frac{1-1/\beta}{\cosh(\alpha)} + \frac{\tanh(\alpha)}{\alpha\beta} - \frac{1}{\beta}\int_0^\beta\frac{\phi}{\phi_o}\,dy^* \\ &- \frac{1}{\beta}\int_0^1\left(\cosh(\alpha y^*) - 1 - \frac{\sinh(\alpha y^*)}{\cosh(\alpha)}(\alpha(\beta-1)+\sinh(\alpha))\right)\left(\frac{\phi}{\phi_o} + \frac{\delta^2}{\alpha^2\varepsilon\varepsilon_o}\frac{\rho_f}{\phi_o}\right)dy^*\Bigg].\end{aligned} \tag{46}$$

Presently, these equations are nondimensionalized in space only. By introducing the scales $\phi^* = \frac{\phi}{RT/F}$, $\rho_f^* = \frac{\rho_f\lambda_D^2}{\varepsilon\varepsilon_o\frac{RT}{F}} = \frac{\rho_f}{2FI_c}$, defining $\gamma = \frac{\lambda_D}{\delta}$, and noting $I_c = \frac{1}{2}\sum_j c_{j,\infty}z_j^2$ is the ionic strength of solution, the quantity contained within the square brackets is converted to dimensionless form,

$$\begin{aligned}\chi_{21}^{(\mathrm{soft})} = -\frac{\varepsilon\varepsilon_o}{\eta}\phi_o\Bigg[&\frac{1-1/\beta}{\cosh(\alpha)} + \frac{\tanh(\alpha)}{\alpha\beta} - \frac{1}{\beta}\int_0^\beta\frac{\phi^*}{\phi_o^*}\,dy^* \\ &- \frac{1}{\beta}\int_0^1\left(\cosh(\alpha y^*) - 1 - \frac{\sinh(\alpha y^*)}{\cosh(\alpha)}(\alpha(\beta-1)+\sinh(\alpha))\right)\left(\frac{\phi^*}{\phi_o^*} + \frac{1}{\alpha^2\gamma^2}\frac{\rho_f^*}{\phi_o^*}\right)dy^*\Bigg].\end{aligned} \tag{47}$$

Last, grouping terms in the final integral into the function $H(y^*;\alpha,\beta)$,

$$\chi_{21}^{(\mathrm{soft})} = -\frac{\varepsilon\varepsilon_o}{\eta}\phi_o\left[\frac{1-1/\beta}{\cosh(\alpha)} + \frac{\tanh(\alpha)}{\alpha\beta} - \frac{1}{\beta}\int_0^\beta\frac{\phi^*}{\phi_o^*}\,dy^* - \frac{1}{\beta}\int_0^1 H(y^*;\alpha,\beta)\left(\frac{\phi^*}{\phi_o^*} + \frac{1}{\alpha^2\gamma^2}\frac{\rho_f^*}{\phi_o^*}\right)dy^*\right], \tag{48}$$

$$H(y^*;\alpha,\beta) = \cosh(\alpha y^*) - 1 - \frac{\sinh(\alpha y^*)}{\cosh(\alpha)}(\alpha(\beta-1)+\sinh(\alpha)). \tag{49}$$

This result succinctly communicates the functional dependence of $\chi_{21}^{(\mathrm{soft})}$ on the physicochemical parameters α, β, and γ and the chemical properties ϕ^* and ρ_f^*.

Four terms contribute to the expression for $\chi_{21}^{(\mathrm{soft})}$. The first two bracketed terms, $\frac{1-1/\beta}{\cosh(\alpha)} + \frac{\tanh(\alpha)}{\alpha\beta}$, represent the direct contribution from the solid charged boundary. This quantity is linearly related to the pressure-normalized velocity gradient at the interface and is only reduced by the presence of the porous layer. The second contribution, $-\frac{1}{\beta}\int_0^\beta \frac{\phi^*}{\phi_o^*}\,dy^*$, is a correction to the previous boundary potential terms resulting from the integration of the normalized potential across the channel. This integral term is minimal when (1) the channel is large relative to the porous layer thickness ($\beta \gg 1$) or (2) the Debye length is small in comparison to all other electrical and boundary length scales in the system ($\gamma \ll 1$, $\gamma \ll \beta$). This term plays an identical role to the integrated potential terms in Eqs. (25) and (28). The final term $-\frac{1}{\beta}\int_0^1 H(y^*;\alpha,\beta)(\frac{\phi^*}{\phi_o^*} + \frac{\rho_f^*}{\phi_o^*}\frac{1}{\alpha^2\gamma^2})\,dy^*$ describes current transport within the porous layer. $H(y^*;\alpha,\beta)$ is a filterlike function that describes the relative penetration of momentum into the porous layer as a function of α and β (or, equivalently, δ, λ_D, and h). This function H is proportional to the pressure-driven velocity within the porous layer, $H(y^*;\alpha,\beta) = \frac{\alpha^2}{G}u_1^{(p)}$. The second term in this integral, $\frac{\phi^*}{\phi_o^*} + \frac{\rho_f^*}{\phi_o^*}\frac{1}{\alpha^2\gamma^2}$, is a modified representation of the free charge density within a porous layer bearing fixed charge.

The behavior of the filterlike function, shown in Fig. 4, is a strong nonlinear function of α and a weak function of β. Here plots of $-\frac{1}{\beta}H(y^*;\alpha,\beta)$ over y^* for varying α and β illustrate the weighting of $\frac{\phi^*}{\phi_o^*} + \frac{\rho_f^*}{\phi_o^*}\frac{1}{\alpha^2\gamma^2}$ at various points in the porous layer. For $\beta = 1$, the porous layer occupies the entire width of the channel, and transport varies from a nearly parabolic flow profile (small α) to a top-hat-like shape dominated by the Brinkman term at large α. For larger values of β and small values of α, transport within the porous layer layer again mimics the portion of the parabolic profile contained in the porous layer. As α increases, the dominant contribution is contributed by the porous layer edge, due to strongly retarded flow toward the interior of the porous layer.

C. χ_{12} with porous and charged interfaces

Although the coupling coefficient $\chi_{12}^{(\mathrm{soft})}$ is identical to $\chi_{21}^{(\mathrm{soft})}$ by Onsager reciprocity, the direct computation of

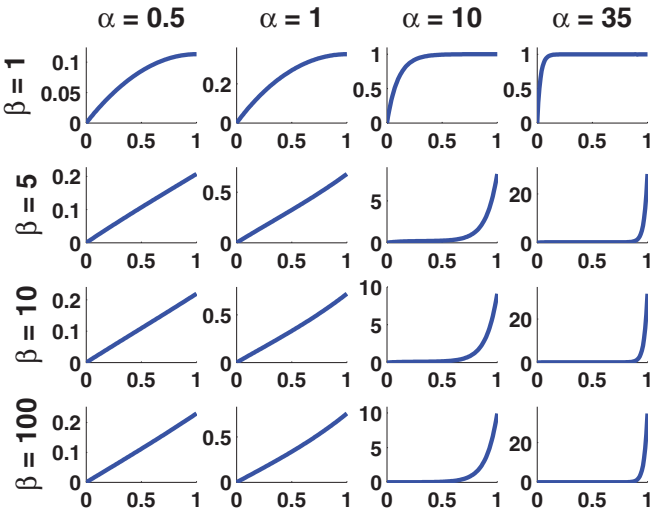

FIG. 4. (Color online) Behavior of the filterlike function $-\frac{1}{\beta}H(y^*;\alpha,\beta)$ as function of space over a range of α (columns) and β (rows). The horizontal axes in all plots range over $0 \leqslant y^* \leqslant 1$.

$\chi_{12}^{(\mathrm{soft})}$ is substantially more difficult than $\chi_{21}^{(\mathrm{soft})}$ because the expressions for electroosmotic flow are more complicated than the corresponding pressure-driven flow relations. The generating formula for $\chi_{12}^{(\mathrm{soft})}$ in our one-dimensional system is

$$\chi_{12}^{(\mathrm{soft})} = -\frac{1}{\beta\langle\nabla\phi_{\mathrm{ext}}\rangle}\int_0^\beta u^{(e)}\,dy^*. \tag{50}$$

The field-driven fluid velocities are computed from the following set of equations:

$$0 = \frac{d^2u_1^{(e)}}{dy^{*2}} - \alpha^2 u_1^{(e)} + \frac{1}{\eta}\frac{d\phi_{\mathrm{ext}}}{dx}\left(\varepsilon\varepsilon_o\frac{d^2\phi}{dy^{*2}} + \delta^2\rho_f\right), \tag{51}$$

$$0 = \frac{d^2u_2^{(e)}}{dy^{*2}} + \frac{1}{\eta}\frac{d\phi_{\mathrm{ext}}}{dx}\varepsilon\varepsilon_o\frac{d^2\phi}{dy^{*2}}, \tag{52}$$

along with the flow boundary conditions from Eq. (6). This set has the solution

$$u_1^{(e)} = C_1e^{\alpha y^*} + C_2e^{-\alpha y^*} - \int_0^{y^*}\frac{\langle\nabla\phi_{\mathrm{ext}}\rangle e^{\alpha y^*}e^{-\alpha s}}{2\alpha\eta}\left(\delta^2\rho_f(s) + \varepsilon\varepsilon_o\frac{d^2\phi}{ds^2}\right)ds + \int_0^{y^*}\frac{\langle\nabla\phi_{\mathrm{ext}}\rangle e^{-\alpha y^*}e^{\alpha s}}{2\alpha\eta}\left(\delta^2\rho_f(s) + \varepsilon\varepsilon_o\frac{d^2\phi}{ds^2}\right)ds, \tag{53}$$

$$u_2^{(e)} = C_3 + y^*C_4 - \frac{\varepsilon\varepsilon_o}{\eta}\langle\nabla\phi_{\mathrm{ext}}\rangle\phi(y^*), \tag{54}$$

with constants

$$C_1 = \frac{1}{2\cosh(\alpha)}\left[\int_0^1\frac{\langle\nabla\phi_{\mathrm{ext}}\rangle}{\alpha\eta}\cosh(\alpha(1-s))\left(\delta^2\rho_f(s) + \varepsilon\varepsilon_o\frac{d^2\phi}{ds^2}\right)ds - \frac{\varepsilon\varepsilon_o}{\alpha\eta}\langle\nabla\phi_{\mathrm{ext}}\rangle\phi_\delta'\right], \tag{55}$$

$$C_2 = -C_1, \tag{56}$$

$$C_3 = \int_0^1 \frac{\sinh(\alpha s)}{\cosh(\alpha)} \frac{\langle \nabla \phi_{\text{ext}} \rangle}{\alpha \eta} \left(\delta^2 \rho_f(s) + \varepsilon \varepsilon_o \frac{d^2 \phi}{ds^2} \right) ds - \frac{\varepsilon \varepsilon_o}{\alpha \eta} \langle \nabla \phi_{\text{ext}} \rangle (\phi_\delta' \tanh(\alpha) - \alpha \phi_\delta), \tag{57}$$

$$C_4 = 0. \tag{58}$$

The coupling coefficient $\chi_{12}^{(\text{soft})}$ follows from a direct integration of the velocity expressions above. The process is tedious but eventually yields the result $\chi_{12}^{(\text{soft})} = \chi_{21}^{(\text{soft})}$. See the Supplemental Material [51] for further details on simplifying $\chi_{12}^{(\text{soft})}$.

VI. ANALYSIS AND LIMITING FORMS OF $\chi_{21}^{(\text{soft})}$ AND $\chi_{12}^{(\text{soft})}$

The coupling coefficients $\chi_{12}^{(\text{soft})}$ and $\chi_{21}^{(\text{soft})}$ (collectively written $\chi_{ij}^{(\text{soft})}$) presented in Eqs. (48) and (49) are superior to alternate forms that depend on free charge, electrical potential slope, and electrical potential concavity terms. Our representation of $\chi_{ij}^{(\text{soft})}$ depends upon quantities that are known exactly in certain regions of the porous layer and are typically straightforward to approximate or bound in the remaining regions. These forms of $\chi_{ij}^{(\text{soft})}$ depend solely on parameters α, β, and γ and spatial distributions of potential (ϕ) and fixed-charge density (ρ_f). Specifically, the fixed charge density may be approximated with information about the chemistry of the charge-generating mechanism. Typically, such bound charge is controlled by pH-dependent chemistry [28,52,53]. Regardless of the charging mechanism, the charge is a nonlinear function of the potential, and estimations of charge densities require estimations of potential, not potential curvature or slope. Using exact, numerical, or approximate expressions for the potential and fixed-charge profiles, these expressions are used as inputs in the function $\chi_{ij}^{(\text{soft})}$. Furthermore, using our form of $\chi_{ij}^{(\text{soft})}$, we obtain physical limits by varying parameters α, β, and γ, absent specific information on the form of the potential and charge distributions.

Our analysis of $\chi_{ij}^{(\text{soft})}$ is informed by the interactions between distributions of momentum, potential, and charge. The Stokes and Poisson equations couple directionally—distributions of charge and potential are unaffected by the transport of momentum, whereas the free-charge distribution strongly affects electroosmotic transport. The quantity α contributes only to hydrodynamics, affecting the degree to which flow is retarded within the porous region. The term γ controls the decay of the potential profile generated by the fixed charge embedded in the porous region and rigid boundary. Although this term does not affect the pressure-driven flow, it does have an effect on the electroosmotic flow. Finally, β contributes to both the momentum and charge distributions by adjusting the separation between momentum and electrical boundary conditions. Furthermore, regions of net free charge (and nonzero potential) are typically confined to the charged porous region plus a distance of several γ's into the pure fluid phase. In general, the parameters α and γ directly control the transport behavior of the system, whereas β indicates the relative magnitude of fluid transport within and outside of the porous region.

We implement analytical approximations and numerical solution methods to resolve the behavior of $\chi_{ij}^{(\text{soft})}$ for varied parameters α, β, and γ. In our analyses, we assume the conventional Boltzmann forcing of the Poisson equation. The Poisson-Boltzmann equation is strongly nonlinear and has no general closed-form solution for our geometry and boundary conditions. Thus, we implement approximate analytical solutions where the potential, ϕ^*, can be estimated. Outside of approximate limits, we perform numerical computations to determine $\chi_{ij}^{(\text{soft})}$.

The parameter $\alpha = \frac{\delta}{\lambda_q}$ determines the penetration of velocity from the pure fluid into the porous region, strongly affecting the value of $\chi_{ij}^{(\text{soft})}$. When $\alpha \to 0$, the resistance of the porous layer is minimal and momentum transfers freely from the fluid into the porous layer; conversely, $\alpha \to \infty$ implies that the porous layer is highly resistive, and transport in the porous layer is throttled. For $\alpha \ll 1$, we perform a series expansion in the small parameter α. Then, to zeroth order in α,

$$\frac{\chi_{ij}^{(\text{soft})}}{-\frac{\varepsilon \varepsilon_o}{\eta} \phi_o} \approx 1 - \frac{1}{\beta} \int_0^\beta \frac{\phi^*}{\phi_o^*} dy^* + \int_0^1 \left(y^* - \frac{y^{*2}}{2\beta} \right) \frac{\rho_f^*}{\phi_o^* \gamma^2} dy^*. \tag{59}$$

Equation (59) shows the limit for $\chi_{ij}^{(\text{soft})}$ in system having a weakly resistive porous layer is equal to the sum of χ_{ij} for a hard surface [the first two terms, which are equivalent to Eq. (25)] and contributions from the fixed-charge-density term (the last integral). Further reducing this expression in the limit of $\beta \gg 1$ removes the second, overlap-correction term. In essence, then, the first *and* third terms are boundary terms, because they are wholly or partially in the limit where reductions by double layer overlap are minimized ($\beta \gg 1$) as follows:

$$\frac{\chi_{ij}^{(\text{soft})}}{-\frac{\varepsilon \varepsilon_o}{\eta} \phi_o} \approx 1 + \int_0^1 \frac{\rho_f^*}{\phi_o^*} \frac{y^*}{\gamma^2} dy^*. \tag{60}$$

All forms of $\chi_{ij}^{(\text{soft})}$ remain bounded even when $\gamma \to 0$ or $\lambda_D \to 0$ in this limit because $\rho_f^* \sim \gamma^2 \sim \lambda_D^2$.

The small-α case offers insight into the importance of the solid-wall potential boundary condition versus the fixed-charge distribution in the porous region. For porous regions thick relative to the Debye length, $\gamma^2 \ll 1$, we expect that the solid boundary will contribute minimally because the wall charge is screened by the charge in the porous layer. For α and $\gamma \ll 1$, $\chi_{ij}^{(\text{soft})}$ is heavily dependent on the porous layer charge, except when the boundary potential greatly exceeds the Donnan potential, $\phi_o^* > \frac{z \sinh(\phi_D^*)}{2z\gamma^2}$. Furthermore, thick porous

layers exhibit minimal concavity in electrical potential far from porous layer edges, $\frac{d^2\phi}{dy^2} \approx 0$, implying $\rho_f^* = \frac{1}{z}\sinh(z\phi_D^*)$ for a z:z electrolyte. Recall that ϕ_D^* is the Donnan potential. For a uniform fixed charge distribution within the porous layer, and using the Donnan potential relationship between charge and potential in the small-γ limit, we obtain:

$$\frac{\chi_{ij}^{(\mathrm{soft})}}{-\frac{\varepsilon\varepsilon_o}{\eta}\phi_o} \approx 1 + \frac{\sinh(z\phi_D^*)}{z\phi_o^*}\frac{1}{2\gamma^2}. \tag{61}$$

As expected, the thick-layer limit of $\chi_{ij}^{(\mathrm{soft})}$ is heavily dependent on the porous layer charge, except when the boundary potential greatly exceeds the Donnan potential, $\phi_o^* > \frac{z\sinh(\phi_D^*)}{2z\gamma^2}$.

When $\beta \to 1$, transport occurs entirely within the porous region, and the only contribution to $\chi_{ij}^{(\mathrm{soft})}$ comes from the porous layer. Applying this condition in Eq. (59) yields, for uniform charge density,

$$\frac{\chi_{ij}^{(\mathrm{soft})}}{-\frac{\varepsilon\varepsilon_o}{\eta}\phi_o} \approx 1 - \int_0^1 \frac{\phi^*}{\phi_o^*}\,dy^* + \frac{1}{3}\frac{\rho_f^*}{\phi_o^*\gamma^2}. \tag{62}$$

The term $\int_0^1 \frac{\phi^*}{\phi_o^*}\,dy^*$ can be approximated as $\frac{\phi_D^*}{\phi_o^*}$ when (1) the wall potential matches identically with the potential in the porous layer (in which case this approximation is exact) or (2) $\gamma \ll 1$, relegating any perturbation in electrical potential to a small region of thickness $\sim 5\gamma$ near the wall. In either case,

$$\frac{\chi_{ij}^{(\mathrm{soft})}}{-\frac{\varepsilon\varepsilon_o}{\eta}\phi_o} \approx 1 - \frac{\phi_D^*}{\phi_o^*} + \frac{1}{3}\frac{\rho_f^*}{\phi_o^*\gamma^2}. \tag{63}$$

Thus, the dominant contribution for a channel completely filled by a porous layer is the charge carried by the porous layer. This limiting area of parameter space implies a zero when $\rho_f^* = 3\gamma^2\int_0^1(\phi^* - \phi_o^*)\,dy$, which can occur only when the porous layer and wall potentials have opposite sign.

Limiting forms of $\chi_{ij}^{(\mathrm{soft})}$ for highly resistive porous layers ($\alpha \gg 1$) are more difficult to obtain than those for weakly resistive porous layers. A uniform limiting expression for the filterlike function $H(y^*;\alpha,\beta)$ is not available for the general case of large α. The difficulty of obtaining approximations of $\chi_{ij}^{(\mathrm{soft})}$ as $\alpha \gg 1$ is well-motivated by Figs. 2 and 4: As α is increased for all $\beta > 1$, flow within the porous layer is zero nearly everywhere *except* the porous layer edge; similarly, $\frac{1}{\beta}H(y;\alpha,\beta)$ tends to zero in all regions but the porous layer edge, where the value of the function increases substantially. The first boundary term, however, can be approximated: The sustained absence of flow near the wall removes the contribution from the boundary term. Given restrictions on interchanging the limit and integration operations for the porous regions integral, we seek further simplifications to χ_{ij} by way of approximation for the quantity $\frac{\phi^*}{\phi_o^*} + \frac{\rho_f^*}{\phi_o^*}\frac{1}{(\alpha\gamma)^2}$. Approximate expressions are delicate at the interface between the porous layer and pure fluid: The potential and fluid velocity both change appreciably in a thin slice of the domain. We begin by considering $\chi_{ij}^{(\mathrm{soft})}$ with $\alpha \gg 1$ and a uniform fixed charge density. Then,

$$\begin{aligned}\frac{\chi_{ij}^{(\mathrm{soft})}}{-\frac{\varepsilon\varepsilon_o}{\eta}\phi_o} \approx& -\frac{1}{\beta}\int_0^\beta \frac{\phi^*}{\phi_o^*}\,dy^* \\ &+ \frac{\rho_f^*}{\phi_o^*}\left(\frac{1}{\alpha^2\gamma^2} + \frac{1/\beta - 1}{\alpha^2\gamma^2\cosh(\alpha)} - \frac{\tanh(\alpha)}{\alpha^3\gamma^2\beta}\right) \\ &- \frac{1}{\beta}\int_0^1 \frac{\phi^*}{\phi_o^*}H(y^*;\alpha,\beta)\,dy^*.\end{aligned} \tag{64}$$

Here terms of $\frac{1}{\alpha^n}$, $n \geqslant 1$, have been omitted; we retain the term $O(\frac{1}{\alpha^2\gamma^2})$ since $\alpha\gamma$ may be of order unity or smaller. In dimensional form, $\alpha\gamma = \lambda_D/\lambda_o$; this combination of parameters controls the local convection of charge at the porous layer edge. This dependence of $\chi_{ij}^{(\mathrm{soft})}$ on $(\alpha\gamma)^{-2}$ results from the coincidence of velocity and potential gradients near the porous layer edge. As λ_D decreases, the potential profile sharpens limiting to a function mimicking the fixed-charge distribution. Similarly, the velocity profile sharpens ($|\frac{du}{dy}|$ increasing) with increasing λ_o at the porous layer edge.

When $\gamma \ll 1$, the potential profile will mimic a step function, and the electrical potential everywhere within the porous layer can be bounded by two limits. Here we estimate the electrical potential ϕ^* in the integral $-\frac{1}{\beta}\int_0^1 \frac{\phi^*}{\phi_o^*}H(y^*;\alpha,\beta)\,dy^*$: (1) a lower bound where the potential everywhere within the porous layer is greater than or equivalent to the potential at the porous layer edge [$\phi^*(1) = \phi(\delta)$ presented in the Supplemental Material [51]], $\phi^* \geqslant \phi_\delta^*$, and (2) an upper bound where the potential everywhere within the porous layer is less than or equal to the Donnan potential of the porous layer, $\phi^* \leqslant \phi_D^*$. Then

$$\begin{aligned}\left.\frac{\chi_{12}^{(\mathrm{soft})}}{-\frac{\varepsilon\varepsilon_o}{\eta}\phi_o}\right|_{\min} =& -\frac{1}{\beta}\frac{\phi_D^* + f(z,\phi_D^*)}{\phi_o^*} \\ &+ \left(\frac{\rho_f^*}{\alpha^2\gamma^2\phi_o^*} + \frac{\phi_D^* + f(z,\phi_D^*)}{\phi_o^*}\right) \\ &\times \left(1 + \frac{1/\beta - 1}{\cosh(\alpha)} - \frac{\tanh(\alpha)}{\alpha\beta}\right),\end{aligned} \tag{65}$$

$$\begin{aligned}\left.\frac{\chi_{12}^{(\mathrm{soft})}}{-\frac{\varepsilon\varepsilon_o}{\eta}\phi_o}\right|_{\max} =& -\frac{1}{\beta}\frac{\phi_D^*}{\phi_o^*} \\ &+ \left(\frac{\rho_f^*}{\alpha^2\gamma^2\phi_o^*} + \frac{\phi_D^*}{\phi_o^*}\right) \\ &\times \left(1 + \frac{1/\beta - 1}{\cosh(\alpha)} - \frac{\tanh(\alpha)}{\alpha\beta}\right).\end{aligned} \tag{66}$$

These relations are compared and evaluated later in Fig. 6(c) for $\alpha \ll 1$ and Fig. 7 for $\alpha \gg 1$. In particular, we apply relations (65) and (66) over the entire range of α in Fig. 8 demonstrating the ability of the expressions to bound $\chi_{ij}^{(\mathrm{soft})}$.

VII. NUMERICAL REPRESENTATION OF $\chi_{ij}^{(\mathrm{soft})}$ FOR ARBITRARY VALUES OF α, β, AND γ, AND VALIDATION OF APPROXIMATE ANALYTICAL FORMULAS

We implement numerical methods to determine $\chi_{ij}^{(\mathrm{soft})}$ outside of the limits described in the previous section. Further,

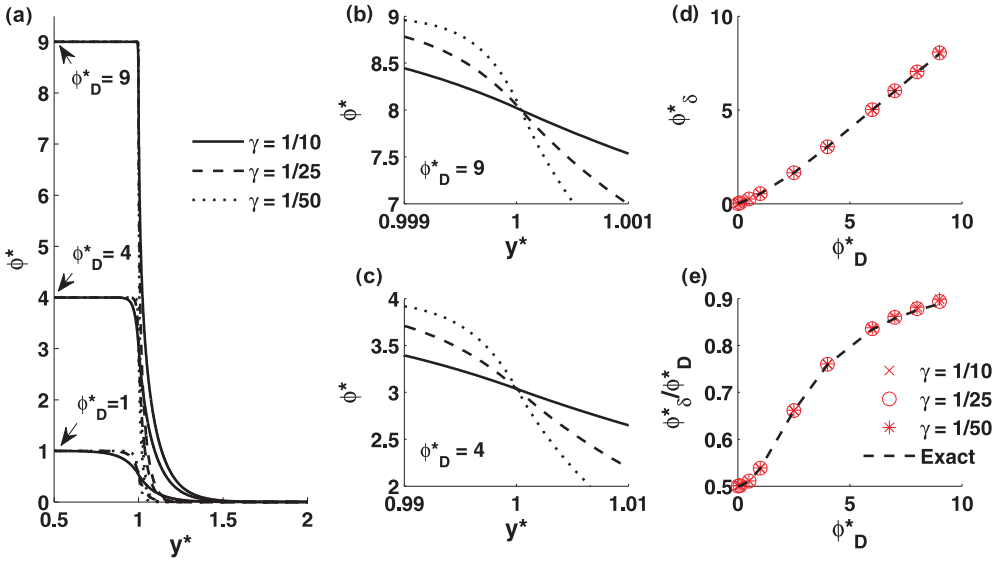

FIG. 5. (Color online) Numerical results for electrical potential distributions and comparison against exact results. For all results, $\beta = 10$ with a 1:1 electrolyte; the uniform porous layer terminates at $y^* = 1$. (a) Potential profiles for various values of potential and γ (as indicated); the extents of the data are truncated to highlight the porous layer edge. Panels (b) and (c) highlight the change in potential near the porous layer edge at $y^* = 1$. The legend in (a) also applies to (b) and (c). (d) and (e) display a comparison between the computed potential at the porous layer edge and the analytical result. The legend in (e) applies to (d) as well.

we use the numerical description of $\chi_{ij}^{(\mathrm{soft})}$ to validate our approximate expressions. We numerically determine $\chi_{ij}^{(\mathrm{soft})}$ in the parameter space spanned by the charge (or potential) in the porous layer and quantities α, β, and γ. We assume the Boltzmann relation for the free charge density. The numerical quadrature of $\chi_{ij}^{(\mathrm{soft})}$ is straightforward if $\phi^*(y^*)$ and $\rho_f^*(y^*)$ are known; this is a main feature of our form for $\chi_{ij}^{(\mathrm{soft})}$—we do not require computations of field gradients, which are prone to numerical errors given the spatially stiff nature of the Poisson-Boltzmann equation. All numerical representations of the potential presume a uniformly charged porous layer, as well as uniform fluid and electrical properties across the entire domain. The details of the numerical scheme are summarized in Ref. [51].

We have compared numerical potential simulations to analytical expressions for the potential at the porous layer edge, with favorable results. At the porous layer edge, we use a Grahame-type formula (see the Supplemental Material [51]) to compare against our numerical calculations. These results, along with potential profiles across the domain for varying values of the parameter γ, are shown in Fig. 5, demonstrating quantitative agreement with theoretical predictions and scaling. As expected, and similarly to the semi-infinite rigid interface solution, the length scale controlling the decay of the potential at the porous layer edge is strongly dependent upon the potential in the porous layer. This decay is illustrated in Fig. 5(a) and shown more clearly in Figs. 5(b) and 5(c). Although Figs. 5(b) and 5(c) are qualitatively similar, the length scale over which Fig. 5(b) decays is 1/10th of the scale in Fig. 5(c). This disparity in decay length is a direct result of the nonlinearity of the governing physics. In contrast to the linearized limit, at large potential the characteristic length scale is a strong function of the local potential. Furthermore, we directly compare numerical and analytical results [cf. Eq. (C9) for the edge potential in the Supplemental Material [51]] in Figs. 5(d) and 5(e), showing excellent agreement. Figures 5(d) and 5(e) demonstrate that the porous layer edge potential matches the analytical result and that the result is invariant to the value of γ. This invariance to γ is also demonstrated in Figs. 5(a) through 5(c). These favorable comparisons establish the validity of our numerical potential simulations to describe the potential and charge distribution within the porous layer system.

Parameters α, β, and γ have distinct effects on the electrokinetic coupling parameters $\chi_{ij}^{(\mathrm{soft})}$. We explored the impact of these parameters on $\chi_{ij}^{(\mathrm{soft})}$ previously with our analytical form (48) and here show a more complete picture via numerics. The parameter α affects only the fluid mechanics of the system. As $\alpha \to \infty$, momentum transport in the porous region vanishes, throttling fluid transport. This restriction occurs independently of the potential profile. The limit of $\alpha \to 0$ represents the opposite extreme, where the porous layer exhibits no resistance beyond fluid viscous effects. For most systems, α is the dominating factor governing the magnitude of the coupling coefficients. This dominance is demonstrated in Fig. 6, showing the cross-coefficients (χ_{12} and χ_{21}) over seven decades of α, while β and γ are simultaneously varied. The results shown in Fig. 6(a) communicate the importance of transport within the porous layer. At low values of α, transport is permitted in the porous region and overall charge transport is enhanced by the coincidence of fluid motion and fixed charge density, with minimal sensitivity to the value of β. All results in Fig. 6 are shown for an interior (or Donnan) potential of $\phi_D^* = 5$, i.e., $\phi_D = 128$ mV. The boundary potential, ϕ_o, is assumed equal to the Donnan potential for these cases.

The selections of $\beta = 1$ and 100 illustrate $\chi_{ij}^{(\mathrm{soft})}$ for a porous layer completely filling the channel ($\beta = 1$) and a porous layer forming a thin region of fixed charge relative to the

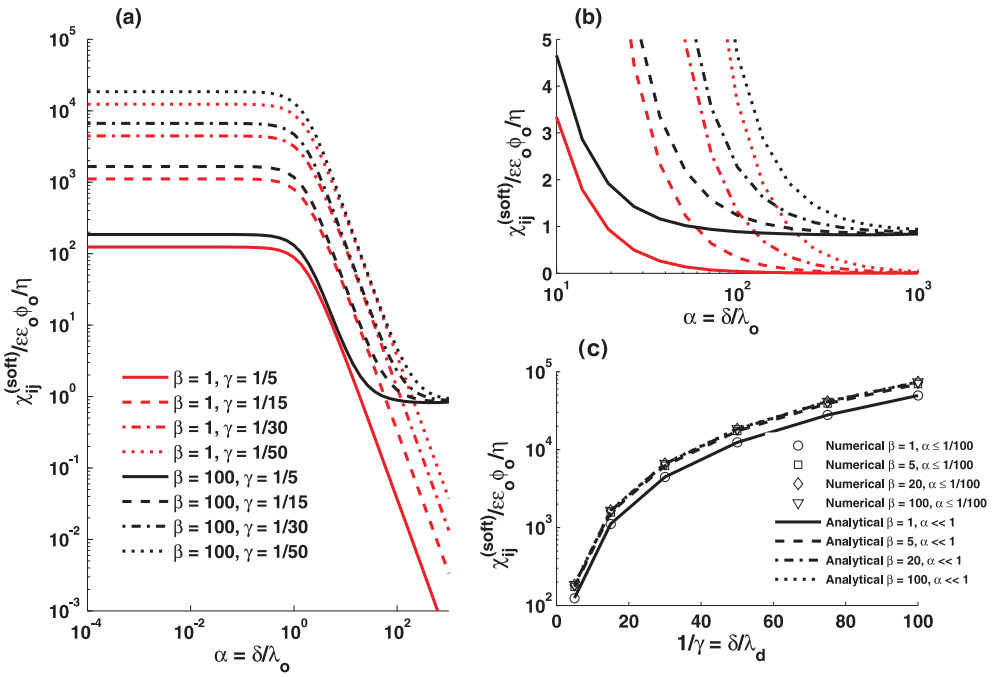

FIG. 6. (Color online) Behavior of the coupling coefficients $\chi_{12}^{(\mathrm{soft})}$ and $\chi_{21}^{(\mathrm{soft})}$ over seven decades of α for $\beta = 1$ [red lines in (a) and (b)], $\beta = 100$ [black lines in (a) and (b)], and various values of γ, indicated with various line styles. Panel (c) compares numerical values and analytical approximations of $\chi^{(\mathrm{hard})}$ in the $\alpha \ll 1$ limit as a function of γ (x axis) and β for $\phi_D^* = 5$, showing excellent agreement.

pure fluid phase ($\beta = 100$). Furthermore, we consider a range of γ indicating porous layers that are similar in size to the Debye length of the fluid (solid lines) to layers that are much larger than the Debye length (dash-dot and dotted lines). The discrepancy between the large- and small-β limit is attributable to convection of charge in the double layer beyond the edge of the porous region. This layer is not present in the $\beta = 1$ limit (as the porous region fills entirely the channel) and thus contributes neither fluid nor current flux. For strongly resistive layers, the data presented in Fig. 6(c) demonstrates that $\chi_{ij}^{(\mathrm{soft})}$ exhibit greater sensitivity to the value of β when α becomes large. Here, the porous layer is strongly resistive and transport occurs mainly in the pure fluid region. For $\beta = 1$, the entire channel is filled with a strongly resistive layer; the flow is throttled, and the fluxes vanish.

The parameter γ affects the coupling coefficients $\chi_{12}^{(\mathrm{soft})}$ and $\chi_{21}^{(\mathrm{soft})}$ at nearly all values of α. When $\alpha \ll 1$, the coupling coefficients reach their limiting maximum form and exhibit a scaling of $1/\gamma^2$. This behavior is shown most clearly in Fig. 6(b), in which the coupling coefficient is plotted as a function of γ for $\alpha \ll 1$, while simultaneously varying the height of the channel (β). The γ^{-2} scaling is confirmed by the favorable comparison between our low-α analytical relation, Eq. (60), and the results of our numerical representations for the potential and coupling coefficients. These results display not only correct scaling but also the accuracy of our analytical approximations in this region.

The value of γ does not affect the limiting result of the coupling coefficients as $\alpha \gg 1$. Rather, the parameter γ controls the value of α at which this limiting result is achieved, as illustrated in Fig. 6(c). This behavior can be explained by considering the potential in regions with fluid transport. For a porous layer with $\alpha \ll 1$, transport occurs near and beyond the porous layer edge, having been diminished within the porous layer. In the context of pressure-driven flow, for the large-α limit, flow is relegated to a thin region of thickness order λ_o near the porous layer edge or α in dimensionless space. Similarly, the fixed charges within the porous layer generate a potential whose decay length is equal to λ_D or γ in dimensionless space. As γ decreases, the potential profile limits to the step function defined by the fixed charge in the porous layer (e.g., Fig. 5). This limiting case exhibits zero potential curvature everywhere in the porous layer *except* at the edge, and within the porous layer the free charge is equal and opposite to the fixed charge. Thus, any transport in this region necessarily depends on both α and γ—increasing values of α will decrease charge transport by reducing fluid velocities at the porous region edge, and decreasing values of γ will increase the charge transport by enhancing the amount of free charge that may be convected near the porous region edge.

Numerical simulations of $\chi_{ij}^{(\mathrm{soft})}$ show that the upper and lower limits for $\chi_{ij}^{(\mathrm{soft})}$ bound the cross-coupling coefficient at large α. Agreement is shown in Fig. 7 for $\alpha = 100$ and $\phi_o^* = 5$ over a range of β and γ. Furthermore, these results communicate that strong changes in the electrical potential profile and transport at the interface are responsible for variations in $\chi_{ij}^{(\mathrm{soft})}$. Both of these effects are apparent when comparing results for $\beta = 1$ to all other cases. When $\beta = 1$, gradients in fluid velocity occur at the solid boundary, and there are no gradients in electrical potential or charge; the approximation matches the numerical data. For $\beta \neq 1$, there is a decay in potential from ϕ_D^* in the porous layer toward the bulk (midline) value; the decay length is governed by the parameter γ. As γ decreases, the dominant flux contribution

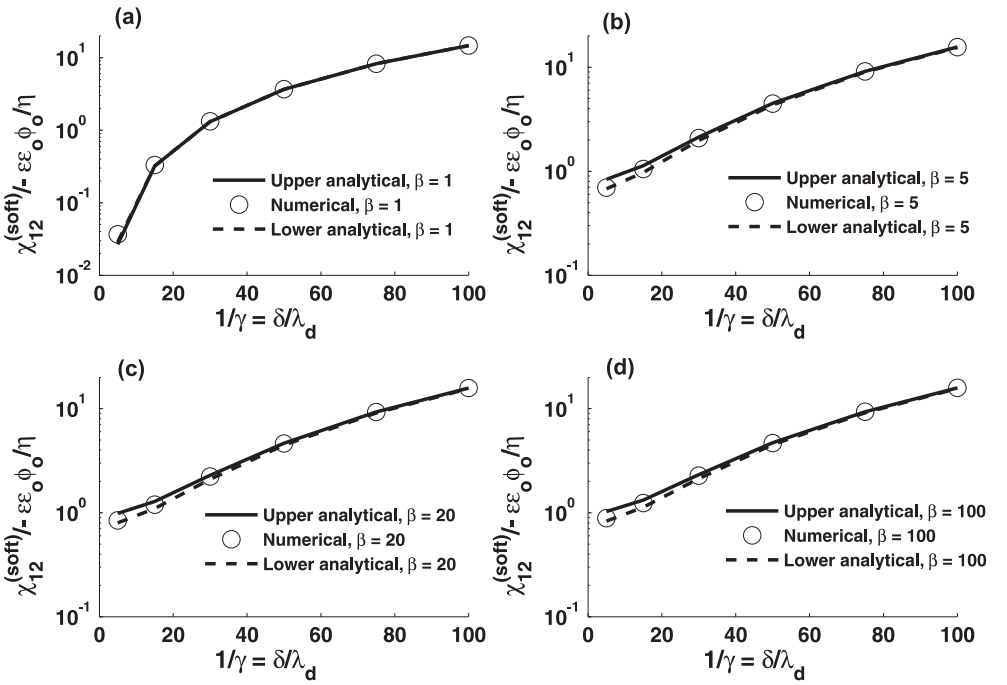

FIG. 7. Upper and lower limit forms of $\chi_{12}^{(soft)}$ for $\alpha = 100$.

is from the value of the fixed charge density. Conversely, when γ becomes large, the potential terms become dominant: Since the potential is estimated everywhere within the porous layer and at the boundary of the porous layer and fluid, the large-γ case yields the largest errors.

Furthermore, the upper and lower bounds derived for $\chi_{ij}^{(soft)}$ at large α [Eqs. (65) and (66)] accurately approximate $\chi_{ij}^{(soft)}$ over a large range of α. This matching, and the associated errors, is shown in Fig. 8. The accuracy of these expressions over the entire range of α is somewhat surprising, as they were developed only for the large-α limit. Given our assumptions on the fixed charge distribution within the porous layer, however, we are able to exactly capture the contribution from each term containing ρ_f^*. Because this fixed charge density term is dominant at low α, the approximation for ϕ^* in the system does not contribute at small α, no matter the accuracy of the estimated value for α. As α is increased, the ϕ^* term in the integral contributes a greater amount as compared to the ρ_f^* term, and the estimated value of the potential in the porous layer *does* play an important role, as seen in Figs. 7 and 8. At large α the exact and approximated values of $\chi_{ij}^{(soft)}$ diverge, producing errors of about 10%.

VIII. CONCLUSION

We have developed simplified analytical expressions for $\chi_{11}^{(soft)}$ and $\chi_{ij}^{(soft)}$ that are functions of known and/or estimable properties of a system with porous and charged layers. These

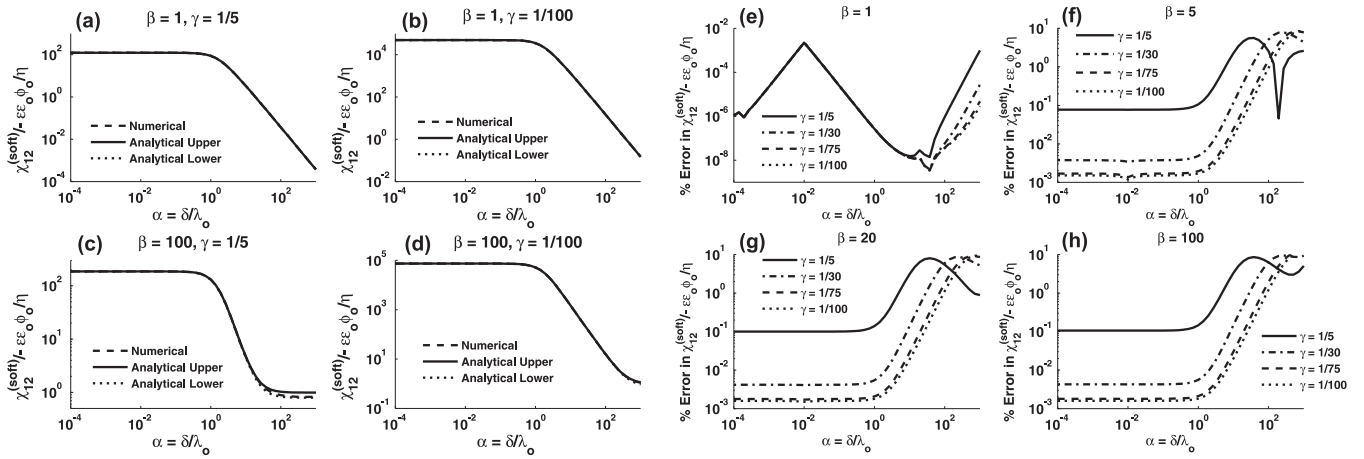

FIG. 8. [(a) through (d)] Large α limit applied over the entire range of α. [(e) through (h)] Errors (as percentages) in $\chi_{12}^{(soft)}$ applied over the entire range of α. The nonmonotonicity observed in the errors is results from taking the maximum error of the difference between the numerical value and upper and lower estimations of $\chi_{ij}^{(soft)}$.

expressions are improvements over earlier works on similar systems by removing the functional dependence on potential curvature and fluid velocity, which are typically not known. Prior workers have examined limiting regions of the parameter space that we consider in full.

Our results consider the limits of system parameters α, β, and γ rather than ϕ_D or ϕ_o, which extends the generality of our results. We have described the system using physical and chemical properties that can be measured or inferred: the solid wall potential (ϕ_o), fixed charge in the porous layer (ρ_f), porous layer thickness (δ), porous layer resistance (k), Debye length (λ_D), the system height (h), and the fluid viscosity (η). These properties can be further reduced to a set to dimensionless parameters, chiefly, the quantities α, β, and γ, which describe distributions of momentum and charge within the system.

With numerical solution of the governing equations, we have validated our approximate analytical forms of the coupling coefficients and have shown that two simple analytical expressions, Eqs. (65) and (66), faithfully describe the behavior of the terms $\chi_{ij}^{(\mathrm{soft})}$ to within 10%. Equations (65) and (66) make no assumptions on the magnitude of the potential or fixed charge density within the porous layer but do assume that the fixed charge is uniformly distributed and the potential deep within the porous layer is gradient-free. Similarly, we have derived and validated expressions for $\chi_{ij}^{(\mathrm{soft})}$ when the parameter α is small, and the small-α limit applies more generally to systems with arbitrary distributions of fixed charge.

The theory, modeling, and analysis herein forms a structure through which systems with porous layers may be analyzed. If system parameters are known, expressions for $\chi_{11}^{(\mathrm{soft})}$ and $\chi_{ij}^{(\mathrm{soft})}$ give predictive capability for several phenomena. Conversely, if the coupling parameters are known from experimental measurements, system parameters may be determined.

ACKNOWLEDGMENTS

The authors acknowledge support from the DOE PECASE program; A.C.B. acknowledges support from the NSF Graduate Research Fellowship Program.

[1] M. A. Swartz and M. E. Fleury, Annu. Rev. Biomed. Eng. **9**, 229 (2007).
[2] A. L. Pidot and J. M. Diamond, Nature **201**, 701 (1964).
[3] E. H. Frank and A. J. Grodzinsky, J. Biomech. **20**, 615 (1987).
[4] E. H. Frank and A. J. Grodzinsky, J. Biomech. **20**, 629 (1987).
[5] T. Ishido and H. Mizutani, J. Geophys. Res. **86**, 1763 (1981).
[6] N. B. McKeown and P. M. Budd, Macromolecules **43**, 5163 (2010).
[7] G. Karimi and X. Li, J. Power Sources **140**, 1 (2005).
[8] R. F. Probstein, *Physicochemical Hydrodynamics* (John Wiley & Sons, New York, 2003).
[9] C. A. Lucy and R. S. Underhill, Anal. Chem. **68**, 300 (1996).
[10] D. Belder and M. Ludwig, Electrophoresis **24**, 3595 (2003).
[11] K. E. Markides, B. J. Tarbet, C. L. Woolley, C. M. Schregenberger, J. S. Bradshaw, M. L. Lee, and K. D. Bartle, J. High Res. Chromotogr. **8**, 378 (1985).
[12] H. Strathmann, Desalination **264**, 268 (2010).
[13] P. G. Saffman, Stud. Appl. Math. **2**, 93 (1971).
[14] G. K. Batchelor, *An Introduction to Fluid Dynamics* (Cambridge University Press, Cambridge, UK, 1967).
[15] L. Onsager, Phys. Rev. **37**, 405 (1931).
[16] L. Onsager, Phys. Rev. **38**, 2265 (1931).
[17] L. D. Landau and E. M. Lifshitz, *Statistical Physics* (Addison-Wesley, Reading, 1958).
[18] S. R. de Groot and P. Mazur, *Non-Equlibrium Thermodynamics* (Dover, New York, 1984).
[19] U. Saxen, Ann. Phys. (Berlin) **47**, 46 (1892).
[20] J. T. G. Overbeek and P. W. O. Wijga, Recl. Trav. Chim. **65**, 556 (2010).
[21] P. Mazur and J. T. G. Overbeek, Recl. Trav. Chim. **70**, 83 (2010).
[22] R. J. Gross and J. F. Osterle, J. Chem. Phys. **49**, 228 (1968).
[23] N. A. Mortensen, L. H. Olesen, F. Okkels, and H. Bruus, Nanosc. Microsc. Thermophys. Eng. **11**, 57 (2007).
[24] S. Wall, Curr. Opin. Colloid Interface Sci. **15**, 119 (2010).
[25] E. Brunet and A. Ajdari, Phys. Rev. E **69**, 016306 (2004).
[26] C. L. A. Berli and M. L. Olivares, J. Colloid Interface Sci. **320**, 582 (2008).
[27] H. P. van Leeuwen and J. F. Duval, J. Colloid Interface Sci. **309**, 350 (2007).
[28] E. Donath and A. Voigt, J. Colloid Interface Sci. **109**, 122 (1986).
[29] H. Ohshima and T. Kondo, J. Colloid Interface Sci. **135**, 443 (1990).
[30] H. Keh and Y. C. Liu, J. Colloid Interface Sci. **172**, 222 (1995).
[31] J. F. L. Duval and H. P. van Leeuwen, Langmuir **20**, 10324 (2004).
[32] J. F. L. Duval, Langmuir **21**, 3247 (2005).
[33] A. C. Barbati and B. J. Kirby, Soft Matter **8**, 10598 (2012).
[34] V. M. Starov and Y. E. Solomentsev, J. Colloid Interface Sci. **158**, 159 (1993).
[35] V. M. Starov and Y. E. Solomentsev, J. Colloid Interface Sci. **158**, 166 (1993).
[36] L. Yezek, J. Duval, and H. van Leeuwen, Langmuir **21**, 6220 (2005).
[37] J. F. L. Duval, R. Zimmermann, A. L. Cordeiro, N. Rein, and C. Werner, Langmuir **25**, 10691 (2009).
[38] R. Zimmermann, D. Kuckling, M. Kaufmann, C. Werner, and J. F. L. Duval, Langmuir **26**, 18169 (2010).
[39] J. F. L. Duval, D. Kuttner, M. Nitschke, C. Werner, and R. Zimmermann, J. Colloid Interface Sci. **362**, 439 (2011).
[40] S. S. Dukhin, R. Zimmermann, J. F. Duval, and C. Werner, J. Colloid Interface Sci. **350**, 1 (2010).
[41] G. S. Beavers and D. D. Joseph, J. Fluid Mech. **30**, 197 (2006).
[42] R. E. Larson and J. J. L. Higdon, J. Fluid Mech. **166**, 449 (2006).
[43] A. S. Sangani and S. Behl, Phys. Fluids A **1**, 21 (1989).
[44] N. Rakotomalala, D. Salin, and Y. C. Yortsos, Appl. Sci. Res. **55**, 155 (1995).
[45] M. F. Tachie, D. F. James, and I. G. Currie, J. Fluid Mech. **493**, 319 (2003).
[46] D. F. James and A. M. Davis, J. Fluid Mech. **426**, 47 (2001).
[47] H. Ohshima and S. Ohki, Biophys. J. **47**, 673 (1985).

[48] B. J. Kirby, *Micro- and Nanoscale Fluid Mechanics Transport in Microfluidic Devices* (Cambridge University Press, Cambridge, UK, 2010).

[49] J. T. Davies and E. K. Rideal, *Interfacial Phenomena* (Academic Press, New York, 1963).

[50] J. Lyklema, *Fundamentals of Interface and Colloid Science: Volume II, Solid-Liquid Interfaces* (Elsevier, Amsterdam, 1995).

[51] See Supplemental Material at http://link.aps.org/supplemental/10.1103/PhysRevE.88.042408 for descriptions of the numerical scheme used, the derivation of χ_{12}^{soft}, and information on various approximations for χ_{ij}^{soft}.

[52] S. S. Dukhin, R. Zimmermann, and C. Werner, J. Colloid Interface Sci. **274**, 309 (2004).

[53] S. S. Dukhin, R. Zimmermann, and C. Werner, J. Phys. Chem. B **111**, 979 (2007).